Structural and optical properties of Er^{3+} ion in sol–gel grown $LiNbO_3$

2007 J. Phys.: Condens. Matter 19 016213

(http://iopscience.iop.org/0953-8984/19/1/016213)

INSTITUTE OF PHYSICS PUBLISHING JOURNAL OF PHYSICS: CONDENSED MATTER

J. Phys.: Condens. Matter **19** (2007) 016213 (14pp) doi:10.1088/0953-8984/19/1/016213

Structural and optical properties of Er^{3+} ion in sol–gel grown $LiNbO_3$

M P F Graça[1], M A Valente[1], M Peres[1], A Cruz[1], M J Soares[1], A J Neves[1], T Monteiro[1], L C Alves[2] and E Alves[2]

[1] I3N, Departamento de Física, Universidade de Aveiro, 3810-193 Aveiro, Portugal
[2] Instituto Tecnológico e Nuclear, ITN, 2686-953 Sacavém, Portugal

Received 25 May 2006, in final form 16 November 2006
Published 7 December 2006
Online at stacks.iop.org/JPhysCM/19/016213

Abstract

Er-doped lithium niobate ($LiNbO_3$) ceramics embedded in silica were grown by the sol–gel method. The dried gel $91SiO_2$–$4Li_2O$–$4Nb_2O_5$–Er_2O_3 (mol%) was subsequently heat treated between 500 and 750 °C. X-ray diffraction and Raman spectroscopy have detected the crystallization of $LiNbO_3$ and $ErNbO_4$ in samples treated at temperatures above 600 °C. At least two Er-related optical centres have been identified by low-temperature optical absorption and photoluminescence studies. The dominant intra-ionic transition arises from the Er^{3+} ion, in C_{2v} site symmetry, in the $ErNbO_4$ lattice.

1. Introduction

Lithium niobate ($LiNbO_3$) is a ferroelectric nonlinear optical material, widely used in integrated and waveguide optics due to its excellent electrical and optical properties [1–3]. Due to the interest in the $^4I_{13/2} \rightarrow {}^4I_{15/2}$ transition, which occurs at $\sim$1.5 μm (a wavelength that matches the minimum absorption of silica-based optical communications systems) a large amount of spectroscopic studies have been performed in Er-doped congruent and stoichiometric $LiNbO_3$ material [4–12]. Site-selective spectroscopy [4–6], x-ray standing wave experiments [7] and electron paramagnetic resonance (EPR) studies [8] have shown the existence of several non-equivalent sites in the $LiNbO_3$ host. Rutherford backscattering and channelling analysis indicates that the Er^{3+} ions preferentially occupy Li^+ sites [9–12] at slightly different off-centre positions but preserving the C_3 point-group symmetry [7, 8].

Doped and undoped $LiNbO_3$ crystal preparation, using conventional routes, is difficult and involves high cost [14–16]; due to this fact, considerable interest has recently been shown in other growth processes such as the vapour transport equilibration method (VTE) [17, 18] and sol–gel routes [19–23]. Glass-ceramic processing, with temperature, atmosphere and time as controllable parameters, is an alternative to sintered ceramics and single-crystal preparation. Dense materials, the control of the shape, size and distribution of the crystalline phases and their

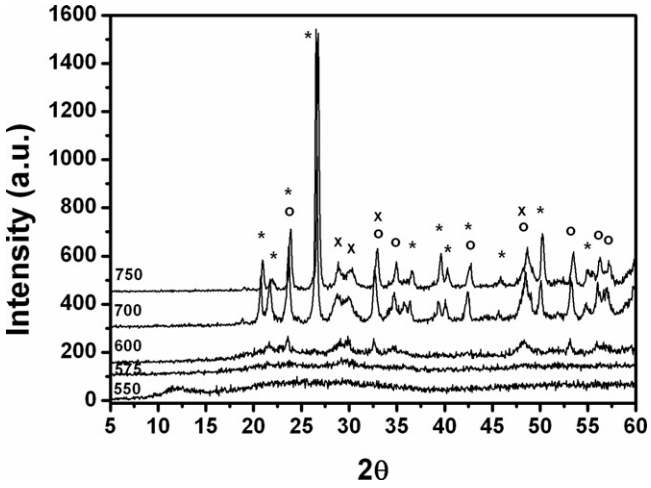

Figure 1. X-ray diffraction patterns of the samples studied: ×—$ErNbO_4$ phase; O—$LiNbO_3$ phase; and ⋆—SiO_2 phase.

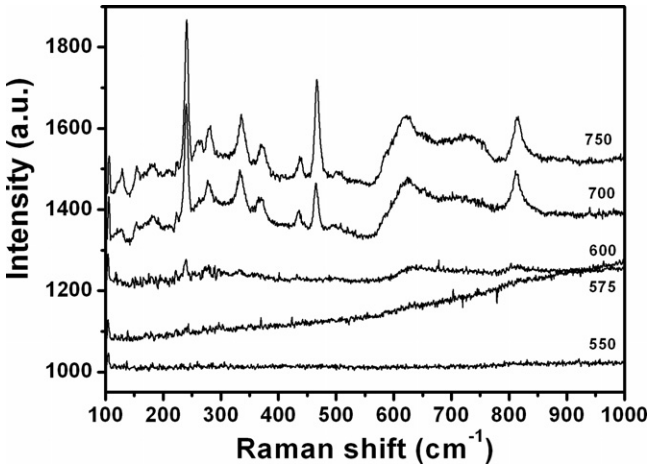

Figure 2. RT Raman spectra of the sol–gel grown and heat-treated $LiNbO_3$:Er samples.

properties can be obtained using this process [19, 20]. The growth of $LiNbO_3$ crystals in a glass matrix is easier and prevents the coarsening and aggregation of crystalline particles. Relative to the melting method, the sol–gel process has the advantages of allowing the synthesis of new glass compositions, with less energy consumption (due to the lower processing temperature), higher purity and better homogeneity of the final product [21–23].

In this work we present results on Er-doped lithium niobate ceramics prepared by heat treating the dried gels of $91SiO_2$–$4Li_2O$–$4Nb_2O_5$–$1Er_2O_3$ (mol%) obtained by the sol–gel route. The x-ray powder diffraction (XRD), Rutherford backscattering spectrometry (RBS), scanning electron microscopy (SEM) and Raman spectroscopy techniques were used to study the composition and structure of the samples. The optical properties were analysed by absorption and photoluminescence (PL) techniques. The effect of the heat treatment on the structural and optical properties of the samples is discussed.

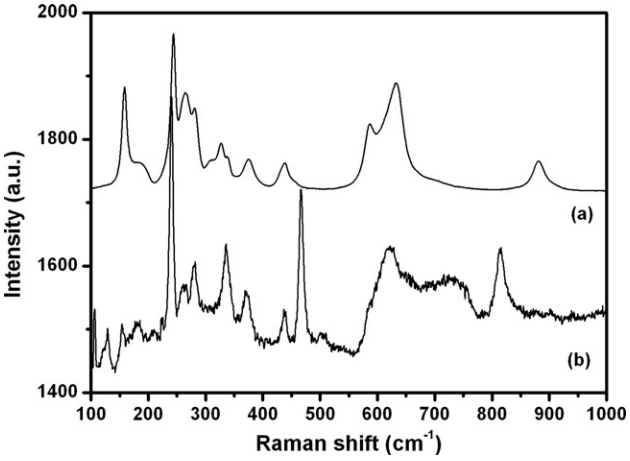

Figure 3. RT Raman spectra of (a) $LiNbO_3$ powder sample and (b) $LiNbO_3$:Er sample grown by sol–gel method and heat treated at 750 °C.

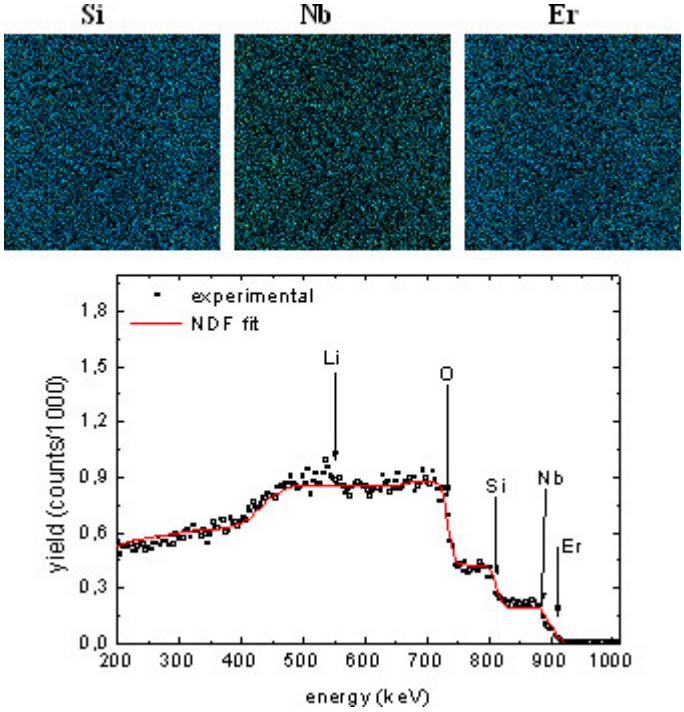

Figure 4. RBS spectrum and composition maps (Si, Nb and Er) obtained with a 1, 5 μm 2.0 MeV H^+ beam for the sample annealed at 750 °C. The maps correspond to a square of 106 μm^2. The continuous curve represents the best fit obtained using the NDF code with a composition $O_{5.23}Si_{2.29}Er_{0.04}Nb_{0.14}Li_{0.14}$.

(This figure is in colour only in the electronic version)

2. Experimental details

The glass of molar composition $91SiO_2$–$4Li_2O$–$4Nb_2O_5$–Er_2O_3 was prepared by the sol–gel route [20, 22] using the following starting materials: tetraethylorthosilicate (TEOS—Merck),

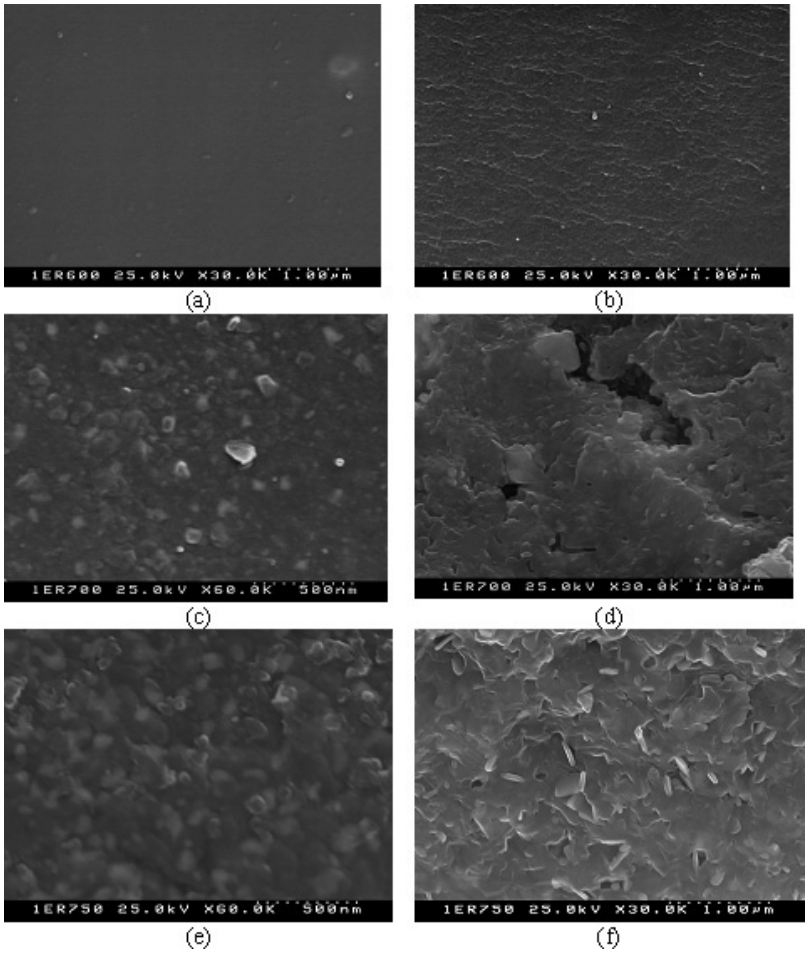

Figure 5. SEM micrographs of the: (a) 600 °C sample surface; (b) 600 °C sample cross section; (c) 700 °C sample surface; (d) 700 °C sample cross section; (e) 750 °C sample surface; (f) 750 °C sample cross section.

ethanol (C_2H_5OH—Merck), lithium nitrate ($LiNO_3$—Merck) niobium chloride (Cl_5Nb—Merck), hydrogen peroxide (H_2O_2 (3% V/V)—Merck) and Erbium nitrate ($Er(NO_3)_3{\cdot}5H_2O$—Merck). The $NbCl_5$ and $LiNO_3$ were dissolved in the hydrogen peroxide solution and added to the TEOS-ethanol solution (1:3 molar ratio). The addition of the $NbCl_5$ changes the pH of the TEOS-ethanol solution from 6 to 1, approximately. The $Er(NO_3)_3{\cdot}5H_2O$ was added to this solution, which was stirred for 1 h at room temperature (RT), poured into Petri dishes and allowed to gel, and dried at 40 °C for 5 days. The molar ratio between TEOS and H_2O was 1:8. The dried gel samples were heat treated, in air, at 120 °C for 48 h. These samples were then heat treated in air for 4 h at six different temperatures (500, 550, 575, 600, 700 and 750 °C) with a heating rate of 75 °C h^{-1}.

The x-ray diffraction (XRD) patterns of powdered samples were obtained at room temperature in a Philips X'Pert system, with Kα radiation ($\lambda = 1.540\,56$ Å) at 40 kV and 30 mA, with a step of 0.05° and a time per step of 1 s. For SEM measurements a conventional Hitachi S4100-1 was used.

Table 1. Raman frequencies of undoped and Er-doped $LiNbO_3$ samples.

	Er:$LiNbO_3$		Pure $LiNbO_3$			
Present work sol–gel	VTE	As grown [29]	Powder VTE $LiNbO_3$ crystal [29]	Nearly stoichiometric $LiNbO_3$ [34]	Theoretical work [35]	Assignments of the modes
261	262	260	260	252	208	A_1 (TO_1)
275	277	275	274	276	279	A_1 (TO_2)
332	333		333	333	344	A_1 (TO_3)
	629	626	629	633	583	A_1 (TO_4)
151.8	153	151	153	152.8	151	E (TO_1)
182	186	182	184	177.3	167	E (TO_2)
237.7	240	238	238	238.3	236	E (TO_3)
261	262	260	260	264.2	307	E (TO_4)
325	323	321	323	321.9	334	E (TO_5)
368	371	367	370	369.5	352	E (TO_6)
433	435	430	433	432.4	432	E (TO_7)
585	584	580	582	580.0	526	E (TO_8)
624	629	626	629	609.8	617	E (TO_9)
308	307	305	305			A_1 (LO)
894	879	877	880			E (LO)
117.8						$ErNbO_4$
124.8						$ErNbO_4$
						SiO_2
465						SiO_2
811.7						$ErNbO_4$

Composition profiles were monitored with RBS (data analysed with NDF code [24]) and particle-induced x-ray emission (PIXE) techniques. H^+ and He^+ microbeams ($\sim$3 μm) were used to scan the sample's surface, and the backscattered particles and x-rays were collected with surface barrier and Si(Li) detectors, respectively. A particle detector with 30 keV energy resolution was placed at 40° with respect to the incident beam in a Cornell geometry.

Raman spectroscopy measurements were performed in backscattering geometry, with the samples at RT, using a T64000 Jobin Yvon spectrometer. A microscope objective (50×) focused the exciting light (Ar^+ laser, $\lambda = 488$ nm) onto the sample (spot diameter $\sim$0.8 μm).

Absorption spectra were measured using a 50 W tungsten lamp, and continuous wave (cw) He–Cd (325 nm) and Ar^+ (488 and 514.5 nm) lasers were used for PL measurements. The samples were mounted in the cold finger of a continuous-flow cryostat, permitting a controlled sample temperature in the range $\sim$7 K to RT. The visible absorption and PL measurements were performed with a Spex 1704 monochromator (1 m, 1200 mm^{-1}) fitted with a cooled Hamamatsu R928 photomultiplier, and the infrared PL measurements were performed with a Brucker 66V Fourier-transform infrared spectrometer equipped with a liquid-nitrogen-cooled germanium detector (North-Coast EO-817).

3. Results and discussion

3.1. Structural and morphological analysis

Figure 1 shows the XRD patterns of the sol–gel prepared glass $91SiO_2$–$4Li_2O$–$4Nb_2O_5$–$1Er_2O_3$ (mol%) after heat treatment at 550, 575, 600, 700 and 750 °C. Increasing the heat

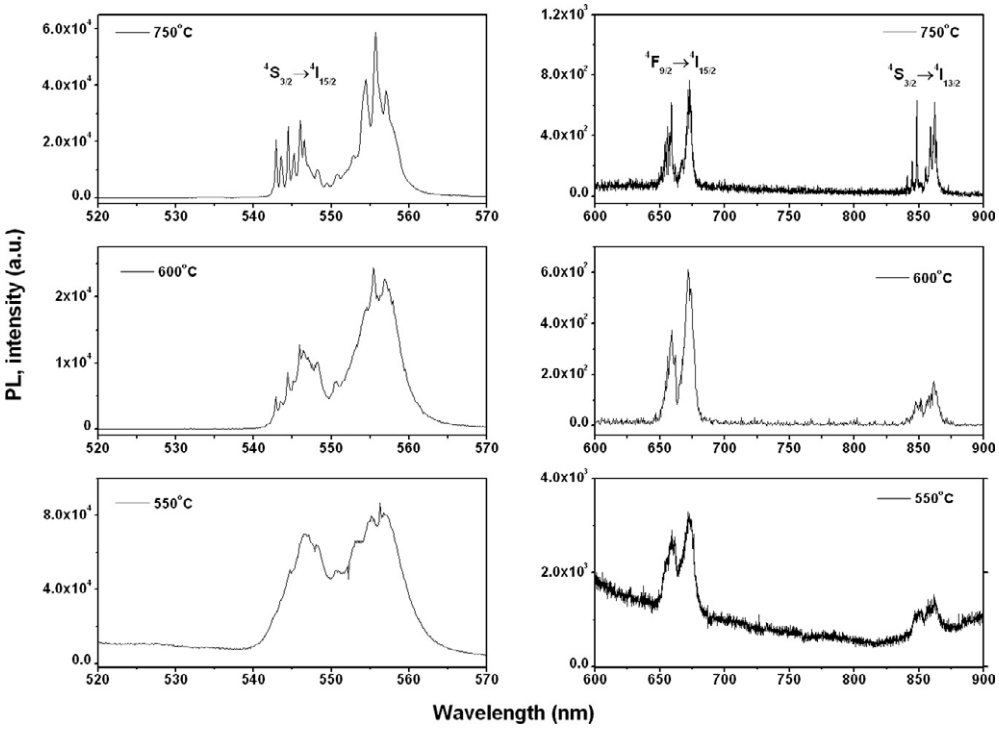

Figure 6. PL spectra at ∼10 K of the $LiNbO_3$:Er samples (heat treated at 550, 600 and 750 °C) obtained with the 488 nm line of an Ar^+ laser.

treatment temperature promotes crystallization, which is reached at temperatures above 600 °C. The first diffraction peaks appear at 600 °C. Samples heat treated above 650 °C show the presence of $LiNbO_3$, $ErNbO_4$ and SiO_2 crystal phases. These data are in agreement with previously observed results reported by Zhang *et al* [17, 18, 25–30] using the VTE growth method. The SiO_2 signal starts to be dominant at 700 °C. The dimensions of the $LiNbO_3$ crystallites, estimated from the measured width of the diffraction peaks using the Scherrer formula [26], are 20.88 ± 0.52 nm (700 °C sample) and 20.47 ± 0.49 nm (750 °C sample). The corresponding sizes of $ErNbO_4$ crystallites are 6.52 ± 0.05 nm and 10.33 ± 0.49 nm, respectively.

Figures 2 and 3 shows typical Raman spectra of the samples analysed. Similar spectra are obtained for different points on the sample surface, indicating good homogeneity of the material produced. As expected, narrow vibrational modes become visible for the samples heat treated above 600 °C, in agreement with x-ray diffraction results.

$LiNbO_3$ crystallize in the trigonal space group $R3c$ ($C_{3v}{}^6$) with two formula units per primitive cell [27–29, 31–33] (a schematic representation of the unit cell of $LiNbO_3$ can be found, for instance, in [11]). The vibrational modes at the centre of the first Brillouin zone transform under the group symmetry operations as $5A_1 + 5A_2 + 10E$ [31]. Three of these modes (A_1, E) are related to the acoustic branches, and the five modes that transform as the A_2 irreducible representations are Raman forbidden [31]. Then the Raman- and infrared-active optical phonon modes with zero wave vector are $4A_1 + 9E$ [27–29, 31–34]. Table 1 lists the observed Raman modes in the samples that were studied and results obtained by

Table 2. Observed transitions at cryogenic temperatures of Er^{3+} ion in the so–gel grown sample heat treated at 750 °C.

	Absorption			Photoluminescence	
$^{2S+1}L_J$ transitions	λ (nm)	E (cm^{-1})	$^{2S+1}L_J$ transitions	λ (nm)	E (cm^{-1})
$^4I_{15/2} \rightarrow {}^4G_{9/2}$	365.8	27 338			
$^4I_{15/2} \rightarrow {}^4G_{11/2}$	378	26 456			
	381	26 248			
	382	26 179			
$^4I_{15/2} \rightarrow {}^2H_{9/2}$	404.7	24 711			
	405	24 692			
	405.3	24 674			
	405.8	24 644			
	407	24 571			
	407.4	24 547			
	407.9	24 517			
	408	25 511			
	409.5	24 421			
	409.7	24 409			
	409.8	24 403			
$^4I_{15/2} \rightarrow {}^2F_{3/2}$	442.9	22 579			
	443.7	22 539			
$^4I_{15/2} \rightarrow {}^2F_{5/2}$	449.6	22 243			
	450	22 223			
	450.6	22 193			
	451.1	22 169			
	451.6	22 144			
	452.1	22 120			
$^4I_{15/2} \rightarrow {}^4F_{7/2}$	485	20 619			
	485.5	29 598			
	485.9	20 581			
	486.4	20 560			
	487.2	20 526			
	487.7	20 505			
	488.2	20 484			
	488.8	20 459			
	489.4	20 434			
$^4I_{15/2} \rightarrow {}^2H_{11/2}$	519.8	19 239	$^2H_{11/2} \rightarrow {}^4I_{15/2}$		
	522.8	19 128			
	524.2	19 077			
	525.2	19 041			
	525.8	19 019			
	526.2	19 005			
				526.2	18 990
				533.5	18 745
				534.6	18 706
				535.1	18 689
				535.8	18 664
$^4I_{15/2} \rightarrow {}^4S_{3/2}$	542.8	18 424	$^4S_{3/2} \rightarrow {}^4I_{15/2}$	542.8	18 424
	543.5	18 400		543.5	18 400
	544.4	18 370		544.4	18 370
	545.2	18 343		545.2	18 343
	546	18 316		546	18 316

Table 2. (Continued.)

	Absorption			Photoluminescence	
$^{2S+1}L_J$ transitions	λ (nm)	E (cm^{-1})	$^{2S+1}L_J$ transitions	λ (nm)	E (cm^{-1})
	546.6	18 296		546.6	18 296
				547.2	18 276
				548.3	18 239
				549.5	18 199
				550.7	18 159
				551.9	18 120
				552.9	18 087
				554.1	18 048
				554.5	18 332
				555.7	17 996
				556.2	17 980
				557.1	17 951
				558.5	17 906
$^4I_{15/2} \rightarrow {}^4F_{9/2}$	647.7	15 440	$^4F_{9/2} \rightarrow {}^4I_{15/2}$		
	648.6	15 418			
	649.2	15 404			
	650.1	15 383			
	651.1	15 359		651.1	15 359
	652	15 338		652	15 338
	652.9	15 317		652.9	15 317
	653.8	15 296		653.8	15 296
	654.1	15 289		654.1	15 289
	654.7	15 275		654.7	15 275
	655.7	15 251		655.7	15 251
	656.9	15 224		656.9	15 224
	657.2	15 217		657.2	15 217
	657.8	15 203		657.8	15 203
	658.1	15 196		658.1	15 196
	659	15 175		659	15 175
	661.5	15 118		661.5	15 118
				666.8	14 998
				669.3	14 942
				672	14 882
				672.9	14 862
				674.3	14 831
$^4I_{15/2} \rightarrow {}^4I_{9/2}$	789	12 675			
	790.5	12 651			
	793	12 611			
	797.2	12 544			
	799.6	12 507			
	802.4	12 463			
	803.8	12 441			
	810.9	12 332			
	811.7	12 321			
	813.3	12 296			
			$^4S_{3/2} \rightarrow {}^4I_{13/2}$	840.3	11 901
				840.8	11 894
				844.4	11 843
				844.8	11 838
				848.3	11 789
				855	11 696

Table 2. (Continued.)

Absorption			Photoluminescence		
$^{2S+1}L_J$ transitions	λ (nm)	E (cm^{-1})	$^{2S+1}L_J$ transitions	λ (nm)	E (cm^{-1})
				857.9	11 657
				858.8	11 645
				860.9	11 616
				862	11 601
				863.3	11 584
			$^4I_{11/2} \rightarrow {}^4I_{15/2}$	980.0	10 204
				983.6	10 167
			$^4I_{13/2} \rightarrow {}^4I_{15/2}$	1532.4	6526
				1537.4	6505
				1540.6	6491
				1543.8	6478
				1553.1	6439
				1561.5	6404
				1585.4	6308
				1612	6204
				1623.6	6159
				1627.6	6144
				1633.8	6121

others [29, 34, 35] in undoped and Er-doped $LiNbO_3$ material. Comparing the phonon frequencies in our sample with the ones in Er-doped material [29] suggests a high Er content.

The physical properties of $LiNbO_3$ depend significantly on the presence of both intrinsic and extrinsic defects. In particular, the Raman spectroscopy is very sensitive to the stoichiometry of the $LiNbO_3$ crystals. Previous Raman investigations showed that when the Li/Nb ratio increases, the full width at half maximum, Γ, of the Raman peak decreases and the peak position does not vary. The linear relation x_C (mol%) = 53.03–0.4739 Γ (cm^{-1}) has been established for the 153 cm^{-1} peak [27, 33], where x_C = [Li]/([Li] + [Nb]). In our 750 °C heat-treated sample, a value of 49.0% was estimated for the x_C Li concentration. The $LiNbO_3$:Er crystals produced using the sol–gel method exhibit a near-stoichiometric composition.

The homogeneity and stoichiometry were also assessed by simultaneous RBS and PIXE analyses. Figure 4 shows a comparison between the experimental RBS spectrum and the simulated spectrum with a composition of $O_{5.23}Si_{2.29}Er_{0.04}Nb_{0.14}Li_{0.14}$. The composition maps obtained with the K x-ray emission for Si and L x-ray emission for Nb and Er reveal a nearly homogeneous distribution of these elements over the scanned area. The RBS spectrum (not shown) with an improved depth resolution, using a $^4He^+$ beam, also indicates an homogeneous depth profile for Er through the first 20 nm of the sample.

Scanning electron microscopy (SEM) was used to analyse the morphology of the sol–gel prepared $LiNbO_3$:Er samples, as shown in figure 5. In the 600 °C annealed sample, the SEM micrographs revealed the presence of a small number of surface particles (figure 5(a)) not observed for the samples annealed at a temperature below 600 °C. The number of surface particles increases with increasing annealing temperature (figures 5(c) and (e)). The sizes of larger particles are similar in both samples and around 100 nm. Comparing the XRD results (figure 1) with the SEM micrographs suggests that these particles result from agglomerates of $LiNbO_3$ crystallites. The cross-section micrographs shows sub micron particles, with a polyhedron-like shape (figures 5(d) and (f)), different from the ones at the surface. The size

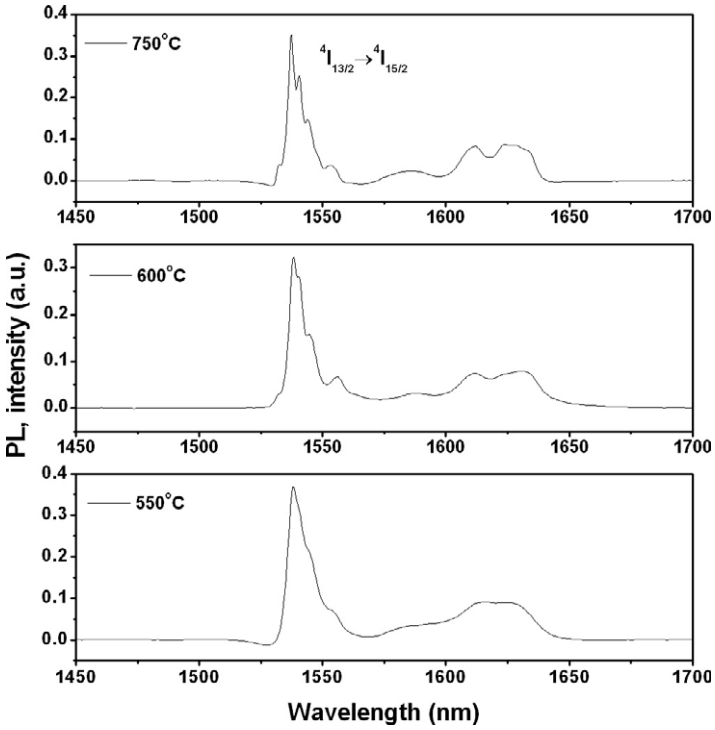

Figure 7. PL spectra at 4.2 K of the $LiNbO_3$:Er samples (heat treated at 550, 600 and 750 °C) obtained with the 488 nm line of an Ar^+ laser.

of these cross-section particles increases with sample heat treatment temperature. Similar behaviour was observed for $ErNbO_4$ crystallite size measured by XRD. We assigned these particles to $ErNbO_4$ crystallites following the similar results of Zhang *et al* [29]. The RBS/PIXE could not resolve these small particles, but the composition maps are coherent with the SEM data. Thus, the heat-treatment process favours $LiNbO_3$ crystallization on the sample surface and $ErNbO_4$ on the bulk.

3.2. Absorption and photoluminescence

Low-temperature visible and infrared PL spectra of the studied samples are shown in figures 6 and 7. As expected, with increasing heat treatment temperature the typical fingerprint lines of the Er^{3+} ion in a crystalline environment are clearly identified. The intra $4f^{11}$ sharp lines start to be observed for temperatures above 600 °C. The sample treated at this temperature only exhibits the $LiNbO_3$ and $ErNbO_4$ crystalline phases. Since no further changes in peak position are detected with increasing temperature, we assume that the rare-earth ion is not incorporated (or not optically active) on the silica matrix.

Figures 8–10 show the low-temperature visible and near-infrared absorption spectra of the 750 °C sample. Transitions from the ground state $^4I_{15/2}$ to the manifolds $^4I_{9/2}$ (∼800 nm), $^4F_{9/2}$ (∼655 nm), $^4S_{3/2}$ (∼545 nm), $^2H_{11/2}$ (∼525 nm), $^4F_{7/2}$ (∼488 nm), $^4F_{5/2}$ (∼451 nm), $^4F_{3/2}$ (∼443 nm), $^2H_{9/2}$ (∼408 nm), $^2G_{11/2}$ (∼382 nm) and $^2G_{9/2}$ (∼366 nm) are clearly observed. The assignments listed in table 2 were made taking into account previous

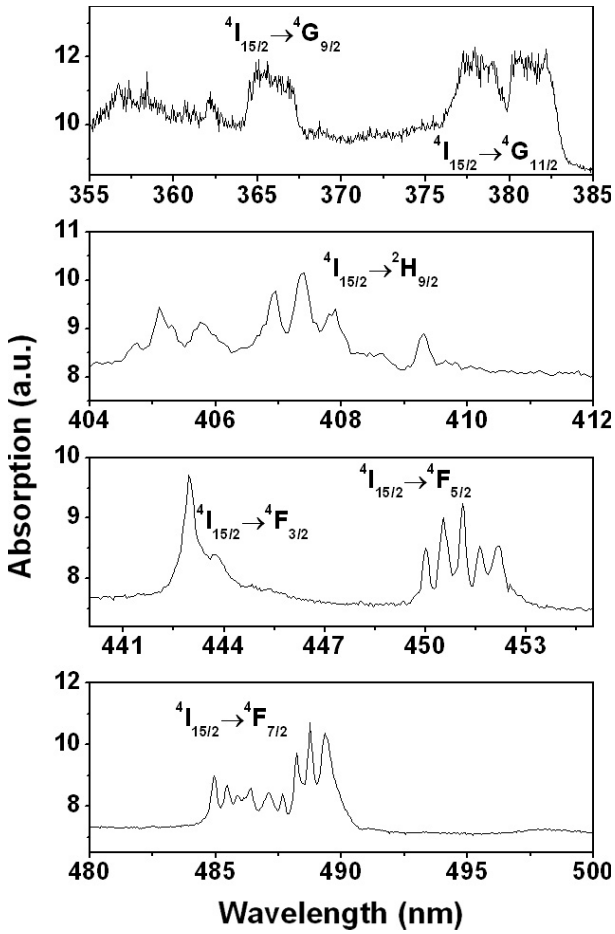

Figure 8. Absorption spectra at ∼10 K of the sol–gel grown $LiNbO_3$:Er sample heat treated at 750 °C.

data [4, 5, 12, 13, 36–39]. With direct pumping on the $^4F_{7/2}$ excited state, six emissions are detected at low temperature, corresponding to the $^2H_{11/2} \rightarrow {}^4I_{15/2}$, $^4S_{3/2} \rightarrow {}^4I_{15/2}$, $^4F_{9/2} \rightarrow {}^4I_{15/2}$, $^4S_{3/2} \rightarrow {}^4I_{13/2}$, $^4I_{11/2} \rightarrow {}^4I_{15/2}$ and $^4I_{13/2} \rightarrow {}^4I_{15/2}$ transitions. These spectra are shown in figures 8 and 9. A total of 12 multiplet manifolds $^{2S+1}L_J$ of Er^{3+} ion were observed. These intra-ionic transitions show a distinct overall structure, such as the number, relative intensities and peak positions of the lines, when compared with previous reported absorption and PL spectra of $LiNbO_3$:Er samples [5, 8, 12, 13, 17, 18]. In contrast, the spectral shape of the observed lines is quite similar to those observed in $ErNbO_4$ samples [39]. Also, more lines than that expected for the Er^{3+} ion in a single site are observed in the low-temperature absorption spectra, assuming that, at ∼10 K, only the lowest sublevel of the ground state is populated. Therefore, the six observed lines for the $^4I_{15/2} \rightarrow {}^4S_{3/2}$ transition suggest the presence of at least three distinct Er sites. However, we cannot exclude that some of the observed absorption lines arise from the other thermally populated sublevels of the ground state. In this case, eight of the observed lines in the PL spectrum must correspond to a single Er site. Nevertheless, the number of downward observed lines still suggests the presence of

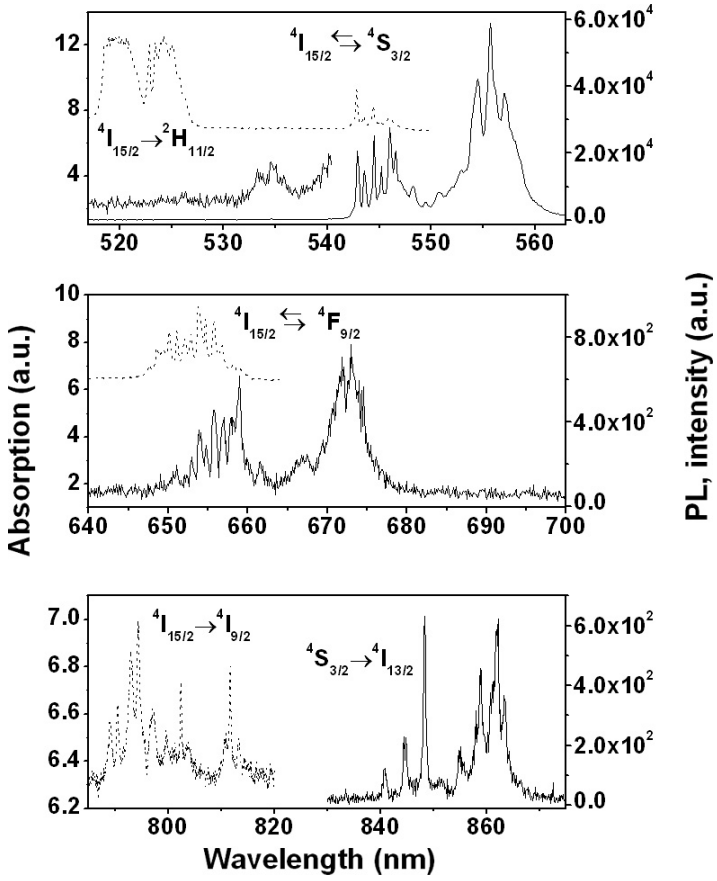

Figure 9. Absorption (dashed lines) and PL spectra (solid lines) at ∼10 K of the sol–gel grown $LiNbO_3$:Er sample heat treated at 750 °C. The PL spectra were obtained with the 488 nm line of an Ar^+ laser.

distinct Er^{3+}-related optical centres. This interpretation is further corroborated by the absence of spectral features using higher excitation energies on the low-temperature PL dependence with excitation energy, shown in figure 11. The unit cell of $ErNbO_4$ crystal is described as pseudo-monoclinic of orthorhombic $Bmm2$ symmetry [40]. A comparison between the spectral features of the Er^{3+} ion in a C_{2v} site symmetry in other hosts [41–43] and the previous reported data on $LiNbO_3$ [5, 8, 12, 13, 17, 18] and $ErNbO_4$ [39] suggests that, in our sol–gel prepared samples, the dominant intra-ionic transitions are due to the Er^{3+} ion in $ErNbO_4$. Cluster sites have been reported as the dominant source of up-conversion [4, 5]. No up-converted light was observed in our samples when pumping the $^4F_{9/2}$ manifold. This suggests that Er clustering is not favoured using the sol–gel growth approach.

4. Conclusions

We have shown that nearly stoichiometric $LiNbO_3$ crystals can be grown using the sol–gel route, heat treating the samples at temperatures above 600 °C. Structural studies show the presence of different crystalline phases, namely $ErNbO_4$ precipitates have been detected.

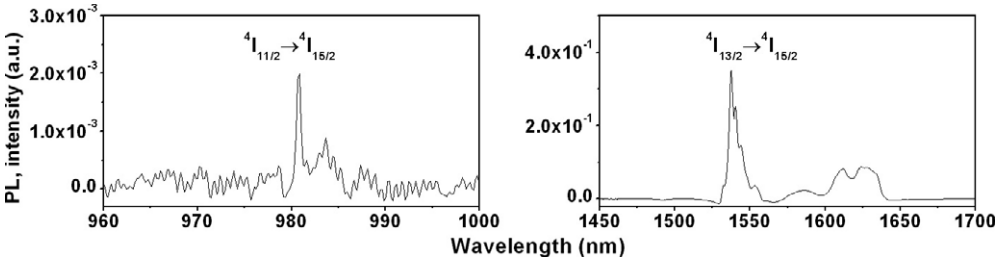

Figure 10. PL spectra at 4.2 K of the sol–gel grown $LiNbO_3$:Er sample heat treated at 750 °C. The PL spectra were obtained with the 488 nm line of an Ar^+ laser.

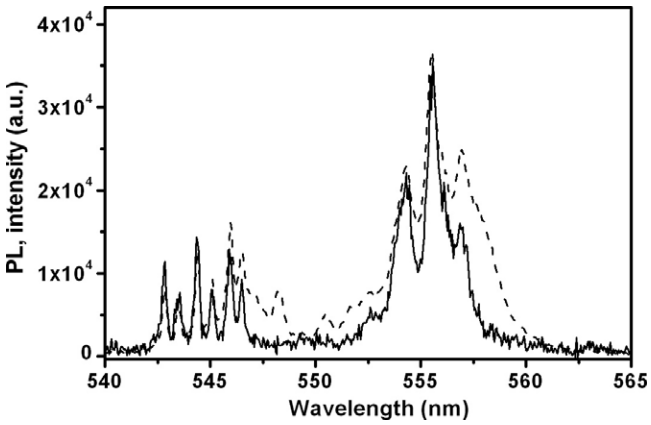

Figure 11. PL spectra at ∼10 K of the sol–gel grown $LiNbO_3$:Er sample heat treated at 750 °C: solid line—PL spectra obtained with the 325 nm line of a He–Cd laser; dashed line—PL spectra obtained with the 488 nm line of an Ar^+ laser.

Low-temperature absorption and PL analysis allow us to identify the Er^{3+} intra $4f^{11}$ transitions arising from at least two optical active centres. The dominant intra-ionic transitions are due to the Er^{3+} ion in a C_{2v} site symmetry in the $ErNbO_4$ lattice.

Acknowledgments

The authors would like to acknowledge financial support by Fundação para a Ciência e Tecnologia (POCTI/CTM/45236/02). M Graça, M Peres, and A Cruz thank the Fundação para a Ciência e Tecnologia for their grants.

References

[1] Becker C, Oesselke T, Pandavenes J, Ricken R, Rochhausen K, Schreiber G, Sohler W, Suche H, Wessel R, Balsamo S, Montrosset I and Sciancalepore D 2000 *IEEE J. Sel. Top. Quantum Electron.* **6** 101
[2] Baumann I, Bosso S, Brinkmann R, Corsini R, Dinand M, Greiner A, Schäfer K, Sochtig J, Sohler W, Suche H and Wessel R 1996 *IEEE J. Sel. Top. Quantum Electron.* **2** 355
[3] Sohler W, Das B K, Dey D, Reza S, Suche H and Ricken R 2005 *IEICE Trans. Electron.* **E88-C** 990
[4] Gill D M, Wright J C and McCaughan L 1994 *Appl. Phys. Lett.* **64** 2483
[5] Witte O, Stolz H and von der Oesten W 1996 *J. Phys. D: Appl. Phys.* **29** 561
[6] Gil D M, McCaughan L and Wright J C 1996 *Phys. Rev.* B **53** 2334

[7] Gog Th, Griebenow M and Materlik G 1993 *Phys. Lett.* A **181** 417
[8] Milori D M B P, Moraes I J, Hernandes A C, de Souza R R, Siu Li M, Terrile M C and Barberis G E 1996 *Phys. Rev.* B **51** 3206
[9] Kovacs L, Rebouta L, Soares J C and da Silva M F 1991 *Radiat Effect. Defects Solids* **119–12** 445
[10] Rebouta L, da Silva M F, Soares J C, Sanz-García J A, Dieguez E and Agulló-López F 1992 *Nucl. Instrum. Methods* B **64** 189
[11] Rebouta L, Smulders P J M, Boerma D O, Agullo-Lopez F, da Silva M F and Soares J C 1993 *Phys. Rev.* B **48** 3600
[12] Herreros B, Lifante G, Cussó F, Sanz J A, Kling A, Soares J C, da Silva M F, Townsend P D and Chandler P J 1998 *J. Phys.: Condens. Matter* **10** 3275
[13] Amin J, Dussardier B, Schweizer T and Hempstead M 1996 *J. Lumin.* **69** 17
[14] Keding K and Rüssel C 1997 *J. Non-Cryst. Solids* **219** 136
[15] Zeng HC, Tanaka K, Hirao K and Soga N 1997 *J. Non-Cryst. Solids* **209** 112
[16] Graça M P F, Valente M A and Silva M G F 2003 *J. Non-Cryst. Solids* **325** 267
[17] Zhang D, Pun E Y B, Chen X, Wang Y, Jin Y, Zhu D and Wu Z 2002 *J. Appl. Phys.* **91** 4014
[18] Zhang D and Pun E Y B 2003 *J. Appl. Phys.* **93** 3141
[19] Todorovic M and Radonjić Lj 1997 *Ceram. Int.* **23** 55
[20] Klein L C 1994 *Sol-Gel Optics: Processing and Applications* (Dordrecht: Kluwer Academic)
[21] Graça M P F, Valente M A and Silva M G F 2002 *Key Eng. Mater.* **230–232** 161
[22] Ferreira da Silva M G and Valente M A 2000 *J. Sol–Gel Sci. Technol.* **17** 47
[23] Graça M P F, Silva M G F and Valente M A 2005 *J. Non-Cryst. Solids* **351** 2951
[24] Barradas N P, Jeynes C and Webb R 1997 *Appl. Phys. Lett.* **71** 291
[25] Zhang D, Lan G, Chen X and Zhu D 2002 *Appl. Phys.* A **74** 265
[26] Zhang D and Pun E Y B 2004 *J. Alloys Compounds* **370** 315
[27] Zhang D, Chen X, Jin Y, Cao X, Zhu D, Wang Y, Ding G, Cui Y, Chen C, Wu Z and Lan G 2001 *Appl. Phys.* A **72** 95
[28] Zhang D, Chen X, Jin Y, Wang Y, Zhu D, Lu B and Lan G 2002 *J. Phys. Chem. Solids* **63** 345
[29] Zhang D, Wang D, Wang Y and Pun E Y B 2004 *Phys. Status Solidi* a **201** 2334
[30] Zhang D, Wong W H and Pun E Y B 2004 *J. Cryst. Growth* **271** 184
[31] Schaufele R F and Weber M J 1966 *Phys. Rev.* **152** 705
[32] Xia H R, Sun S Q, Cheng X F, Dong S M, Xu H Y, Gao L and Cui D L 2005 *J. Appl. Phys.* **98** 33513
[33] Schlarb U, Klauer S, Wesselmann M, Betzler K and Wöhlecke M 1991 *Appl. Phys.* A **56** 311
[34] Ridah A, Bourson P, Fontana M D and Malovichko G 1997 *J. Phys.: Condens. Matter* **9** 9687
[35] Caciuc V, Postnikov A V and Borstel G 2000 *Phys. Rev.* B **61** 8806
[36] Zhang D, Pun E Y B, Chen X, Wang Y, Jin Y, Zhu D and Wu Z 2002 *J. Appl. Phys.* **91** 4014
[37] Zhang D and Pun E Y B 2003 *J. Appl. Phys.* **93** 3141
[38] Gruber J B, Sardar D K, Yow R M and Zandi B 2004 *Phys. Rev.* B **69** 195103
[39] Zhang D, Wang Y, Pun E Y B, Yu Y, Chen C and Yao J 2004 *Opt. Mater.* **25** 379
[40] Sternberg A, Shebanovs L, Yamashita J Y, Antonova M, Livinsh M and Shorubalko I 1999 *Ferroelectrics* **224** 565
[41] Choe S, Park H and Kim W 2000 *J. Appl. Phys.* **88** 6089
[42] Maeda N, Wada N, Onoda H, Maegawa A and Kojima K 2003 *Thin Solid Films* **445** 382
[43] Wilson B A, Yen W M, Hegarty J and Imbusch G F 1979 *Phys. Rev.* B **19** 4238